Nano-Micro Letters

ISSN 2311-6706
e-ISSN 2150-5551
CN 31-2103/TB

ARTICLE

https://doi.org/10.1007/s40820-020-0398-2

Cite as
Nano-Micro Lett.
(2020) 12:55

Received: 23 October 2019
Accepted: 2 January 2020

Sandwich-Like Fe&TiO_2@C Nanocomposites Derived from MXene/Fe-MOFs Hybrids for Electromagnetic Absorption

Baiwen Deng[1], Zhen Xiang[1], Juan Xiong[1], Zhicheng Liu[1], Lunzhou Yu[2], Wei Lu[1] ✉

✉ Wei Lu, weilu@tongji.edu.cn

[1] Shanghai Key Lab. of D&A for Metal-Functional Materials, School of Materials Science & Engineering, Tongji University, Shanghai 201804, People's Republic of China

[2] School of Materials Science & Engineering, University of Shanghai for Science and Technology, Shanghai 200092, People's Republic of China

HIGHLIGHTS

- Sandwich-like laminated Fe&TiO_2@C nanocomposites were successfully prepared from the MXene–MOFs hybrids.
- A broad effective bandwidth of 6.5 GHz at a thickness of only 1.6 mm was achieved.

ABSTRACT Electromagnetic pollution has been causing a series of problems in people's life, and electromagnetic absorbers with lightweight and broad absorbing bandwidth properties are widely desired. In this work, novel sandwich-like 2D laminated Fe&TiO_2 nanoparticles@C nanocomposites were rationally designed and successfully developed from the MXene–MOFs hybrids. The formation of Fe and rutile-TiO_2 nanoparticles sandwiched by the two-dimensional carbon nanosheets provided strong electromagnetic energy attenuation and good impedance matching for electromagnetic wave (EMW) absorption. As expected, the nanocomposites achieved a broad effective absorption bandwidth of 6.5 GHz at a thickness of only 1.6 mm and the minimum reflection loss (*RL*) value of − 51.8 dB at 6.6 GHz with a thickness of 3 mm. This work not only provides a good design and fabricating concept for the laminated metal and functional nanoparticles@C nanocomposites with good EMW absorption, but also offers an important guideline to fabricate various two-dimensional nanocomposites derived from the MXene precursors.

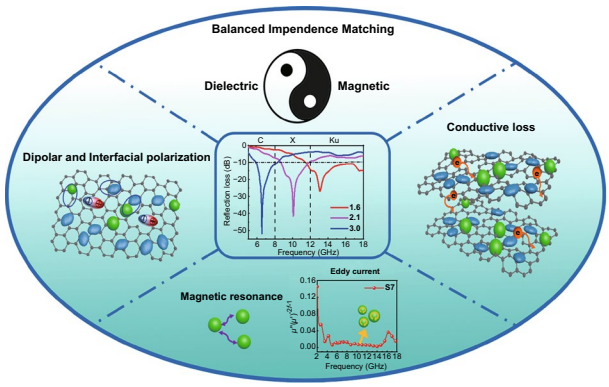

KEYWORDS MXene; Metal–organic frameworks; Nanocomposites; Electromagnetic wave absorption

1 Introduction

With the surging development of electrical communication devices, an extensive increase in hazardous electromagnetic radiation and interferes has become a severe problem in both civil and precision technical fields. Therefore, there is a great demand for developing broadband and high-efficiency electromagnetic wave (EMW) absorbing materials to minimize adverse effects in aspects of health and electrical devices [1–3]. Abundant efforts have been contributed to the development of high-efficiency EMW absorbers with a broad effective absorption bandwidth (EAB), especially for the radar frequency range of 2–18 GHz [4–6]. In general, materials with laminated structure are well known as promising

Published online: 18 February 2020

EMW absorbers. Due to the unique layered structure of these laminated materials, which possess large surface area and heterogeneous interfaces, abundant dipolar, and interfacial polarizations could be generated during EMW absorption process. This is believed to be the main contribution to the excellent EMW absorbing ability [7–9]. Specifically, the most widely studied laminated EMW absorbers was the graphene-based two-dimensional materials in the past decade [2, 9–11]. Since the EMW absorption ability of graphene or reduced graphene oxide (RGO) nanosheets was not ideal, assembling functional particles with graphene or RGO has become a promising way to improve their performance, such as Ni/graphene [12], Co_3O_4–rGO [13], and ZnO–rGO [14].

MXene is a new family member of the big family tree of two-dimensional (2D) materials [15, 16], whose formula is $M_{n+1}X_nT_x$, where M is an early transition metal, X is carbon and/or nitrogen, and T_x is the surface terminations usually −OH, –F, and/or –O [17–19]. Due to the laminated structure and unique combination of electrical conductivity and hydrophilicity, MXene is considered as an attractive candidate for various applications, including energy storage [16, 20, 21], sensors [22, 23], electromagnetic absorption, and electromagnetic interference shielding [3, 8, 24, 25]. Feng et al. [8] synthesized $Ti_3C_2T_x$ nanosheets by HF system etching process, which appeared enhanced microwave absorption ability (*RL* value of −40 dB at 2 mm thickness). Xu et al. [26] achieved a $Ti_3C_2T_x$ with a *RL* value of −41.9 dB at 13.4 GHz and thickness of only 1.1 mm by solvothermal treatment. Luo et al. [5] demonstrated a wide absorbing bandwidth (*EAB* over 10 GHz at a thickness of 3 mm) in $Ti_3C_2T_x$ MXene absorbers. $Ti_3C_2T_x$ is a representative of MXene family decorated with abundant active surface functional terminations [27–29], which could provide remarkable amount of dipolar and interfacial polarizations. Moreover, the variety surface terminations of MXene by ion intercalation [30], annealing [31], and oxidization [32] could offer tunable EMW absorbing properties. In general, EMW absorbers should have strong EM energy attenuation ability and moderate conductivity for impedance matching. However, the high electrical conductivity of $Ti_3C_2T_x$ could be a big obstacle for the application as EMW absorbers [32]. Generally, the combination of magnetic particles and conductive carbon materials is considered as an effective way to achieve an improved EMW absorption by improving the impedance matching [33, 34]. Therefore, assembling the magnetic nanoparticles with the MXene oxides, such as $TiO_2/Ti_3C_2T_x/Fe_3O_4$ [6], NiO&TiO_2@C [35], C/TiO_2/α–Fe [36], and Co/TiO_2@C [37], could effectively improve the impedance matching with little cost of its EMW energy attenuation performance. In summary, integrating magnetic particles with oxidized MXene could be a promising and effective way to obtain high-performance EMW absorption materials by optimizing the impedance matching.

The magnetic particles could be derived from novel metal organic framework (MOFs) materials [38–41]. Owing to their unique porous structures, MOFs are considered as ideal precursors for preparing nanostructured metal@C nanocomposites through facile heat treatment methods and provide intriguing electromagnetic (EM) absorption properties [42–45]. For instance, Zhou et al. [44] fabricated hierarchical MOF-derived Co/C@V_2O_3 hollow spheres with an enhanced EMW absorption performance (RL_{min} of −40.1 dB and EBW of 4.64 GHz at a thickness of 1.5 mm). Liu et al. [46] synthesized porous carbon-wrapped Ni composites from Ni-based MOF with high EMW absorption performance (RL_{min} of −51.8 dB and an EBW of 3.48 GHz at a thickness of 2.6 mm). Lü et al. [47] provided a porous Co/C nanocomposite derived from ZIF-67 (a kind of Co-based MOF), which achieved a broad EBW of 5.8 GHz with a RL_{min} value of −35.3 dB. Li et al. [48] also successfully prepared hollow Co/C microspheres from ZIF-67, which exhibited a high RL_{min} of −66.5 dB. Thus, the combination of 2D materials and MOFs derived magnetic particles could be a solution for achieving high-performance and broadband EMW absorbers. Though there are numerous works about introducing magnetic materials into MXene as mentioned, the EMW absorbers fabricated by in situ MXene–MOFs hybrids have been rarely studied [3, 37].

Herein, we demonstrate a facile route toward the rational construction of sandwich-like 2D laminated Fe&TiO_2 nanoparticles@C nanocomposites derived from MXene/Fe-MOFs hybrids through a rapid microwave-assisted heating reaction followed by a suitable heat treatment. The in situ generated Fe and TiO_2 nanoparticles embedded closely into each MXene-derived carbon nanolayers to form a two-dimensional sandwich-like laminated structure. The results indicate that the 2D laminated nanocomposites exhibit excellent tunable EMW absorption performance with high reflection loss (RL_{min} of −51.8 dB), lightweight (a matching thickness of 1.6 mm), and broad bandwidth (6.6 GHz) due to the plentiful interfacial polarization and other mechanisms of EMW attenuation. Furthermore, our work offers

https://doi.org/10.1007/s40820-020-0398-2

an important facile approach to fabricate two-dimensional nanocomposites derived from MXene–MOF hybrids along with a good design and fabricating concept for the laminated metal and functional nanoparticles@C nanocomposites with good EMW absorption.

2 Experimental Section

2.1 Raw Materials

In this work, all chemical reagents were of analytical grade and not further purified. Specifically, hydrochloric acid (HCl), lithium fluoride (LiF), *N*,*N*-dimethylformamide (DMF), 1,4-benzenedicarboxylic acid (H_2BDC), and ferric chloride hexahydrate ($FeCl_3{\cdot}6H_2O$) were purchased from Shanghai Aladdin Industrial Corporation. Ti_3AlC_2 powders (> 98 wt% purity) were purchased from Laizhou Kai Kai Ceramic Materials Co., Ltd.

2.2 Preparation of $Ti_3C_2T_x$-MXene

$Ti_3C_2T_x$ MXene was synthesized by removing Al atoms in Ti_3AlC_2 precursor based on the typical LiF–HCl etching method [19]. Firstly, 0.5 g of LiF was added into the concentrated 12 M HCl solution. Secondly, the solution was stirred 10 min with a magnetic Teflon stir to dissolve the LiF completely. Then, 0.5 g of Ti_3AlC_2 was slowly added into the solution and stirred at 50 °C for 24 h. The resultant suspension was washed by deionized water for several times via centrifugation process (3500 rpm, 5 min for every washing circle) until the pH value of supernatant became 5–6. Finally, the obtained $Ti_3C_2T_x$ sediments were collected and dried in a vacuum oven for 24 h.

2.3 Preparation of MXene–MOF Hybrids

The 0.12 g of as-prepared $Ti_3C_2T_x$ MXene was added into 20 mL of N,N-dimethylformamide (DMF) and then sonicated for 30 min to form a uniform black solution. After that, 0.5405 g of $FeCl_3{\cdot}6H_2O$ was dissolved in the solution with sonication for 30 min. The 0.3323 g of terephthalic acid was dissolved into the $Ti_3C_2T_x$ and Fe^{3+} mixture by vigorously stirring for 30 min. After that, 0.8 mL of 2 M NaOH solution was added dropwise into the mixture with ongoing stirring. Then, the as-prepared mixture was transferred into a 100-mL three-neck boiling flask. Following that, the reaction was conducted at 100 °C for 30 s in a microwave heating equipment. The obtained black solution was centrifuged and washed by DMF, deionized water, and ethanol. The resulting black product was dried in a vacuum oven for 3 h. The mass of resultant $Ti_3C_2T_x$–Fe-MOFs hybrids was 0.26 g, indicating the mass ratio for $Ti_3C_2T_x$ and Fe-MOFs was about 1.2.

2.4 Preparation of Fe&TiO_2@C Composites

The MXene–MOF hybrids obtained as above were carbonized at 700 °C for 2 h with a heating rate of 10 °C s^{-1} under a H_2/Ar atmosphere. This product will be referred as S7. To ascertain the influences of structure modification on EMW absorption ability, the MXene–MOF hybrids were also carbonized at 600 and 800 °C under the same atmosphere condition, which will be referred as S6 and S8, respectively.

2.5 Characterization

The thermogravimetric and differential scanning calorimetry (TG/DSC) curves of MXene–MOF hybrids were obtained to help understanding the transforming process from $Ti_3C_2T_x$–Fe-MOF hybrids to Fe&TiO_2@C composites, by using a thermal analysis system at the temperature range from 30 to 850 °C under N_2 atmosphere. X-ray diffraction (XRD) patterns of the obtained S6, S7, S8, and $Ti_3C_2T_x$ samples were recorded by X-ray diffractometer equipped with CuK_α radiation from 4° to 65° (a step scan of 0.02° and 1 s per step). Raman tests were carried out on a Raman microspectrometer with a He–Ne laser. The magnetic properties of the composites were measured by vibrating sample magnetometer (VSM, Lake Shore7307). The morphologies of the precursor and obtained powders were characterized by a transmission electron microscope (TEM) and a scan electron microscope (SEM).

To measure complex permittivity and complex permeability, paraffin was chosen as the matrix material due to its small contribution to dielectric and magnetic properties. S6, S7, and S8 samples were dispersed into the paraffin with loading ratio of 40 wt%. Finally, the well-mixed mixtures were molded into a torus-shape (3.04 mm of inner diameter and 7.00 mm of outer diameter) test samples. The complex permittivity and complex permeability were measured using

an Agilent N5224A vector network analyzer in the frequency range from 2 to 18 GHz.

3 Results and Discussion

3.1 Synthesis of Fe&TiO_2@C Nanocomposites

The detailed fabrication process of the sandwich-like two-dimensional laminated Fe&TiO_2 nanoparticles@C nanosheets composites is illustrated in Fig. 1. Firstly, the 2D laminated MXene nanosheets were synthesized based on a typical LiF-HCl etching method. Then, the $Ti_3C_2T_x$–Fe-MOFs hybrids were facilely synthesized by the microwave-assisted heating process using $FeCl_3{\cdot}6H_2O$, terephthalic acid, and NaOH as reactants in a DMF solution. During the reaction process, Fe^{3+} ions, which were inserted in or absorbed on the layers of $Ti_3C_2T_x$, could form a shuttle-like Fe-MOFs by coordinating the carboxylate groups of terephthalic acid by strong metal–ligand bonds [49]. Finally, the sandwich-like two-dimensional Fe&TiO_2@C nanocomposites were obtained via the carbonization of the $Ti_3C_2T_x$–Fe-MOFs hybrids at high temperature for 2 h in H_2/Ar atmosphere. In the carbonization process, shuttle-like Fe-MOFs have been transformed into Fe nanoparticles covered with carbon. At the same time, the TiO_2 nanoparticles and laminated carbon nanosheets were in situ generated from the $Ti_3C_2T_x$. Therefore, this transformation process provided a novel sandwich-like two-dimensional laminated structure of Fe&TiO_2@C nanocomposites, in which the layered carbon nanosheets were filled with the Fe and TiO_2 nanoparticles.

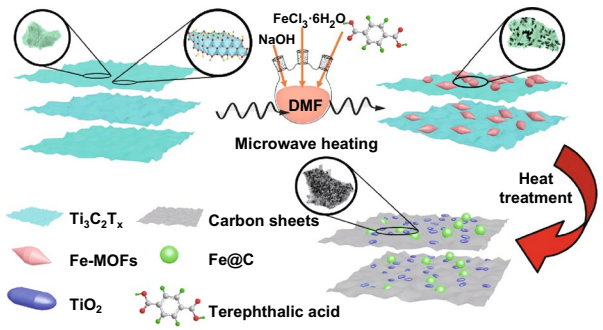

Fig. 1 Schematic representation of the facile synthesis route of the Fe&TiO_2@C by the EMW heating reaction followed by a heat treatment

3.2 Microstructure

The TG curve of the $Ti_3C_2T_x$–Fe-MOF hybrids is shown in Fig. 2a, while the DSC result is exhibited in Fig. S1. Three significant weight loss processes were observed from the TG curve. The first process, ranging from 30 to 110 °C, could be considered as a weight loss process for the non-combined water in hybrids. The following weight loss at temperature range of 115 to 340 °C was attributed to the loss of the combined water and surface functional groups [32]. The total weight loss from 30 to 340 °C was 18.2%. Another weight loss occurred at the temperature range of 340 to 570 °C, which accompanied with an exothermic peak at 400 °C, might be attributed to the carbonization of Fe-MOF and $Ti_3C_2T_x$. It was worth noting that a sharp exothermic peak was found at 566 °C in the DSC curve, which could be the result for phase transformation from anatase to rutile. The XRD patterns of the as-prepared $Ti_3C_2T_x$ and $Ti_3C_2T_x$–Fe-MOFs hybrids carbonized at 600, 700, and 800 °C are

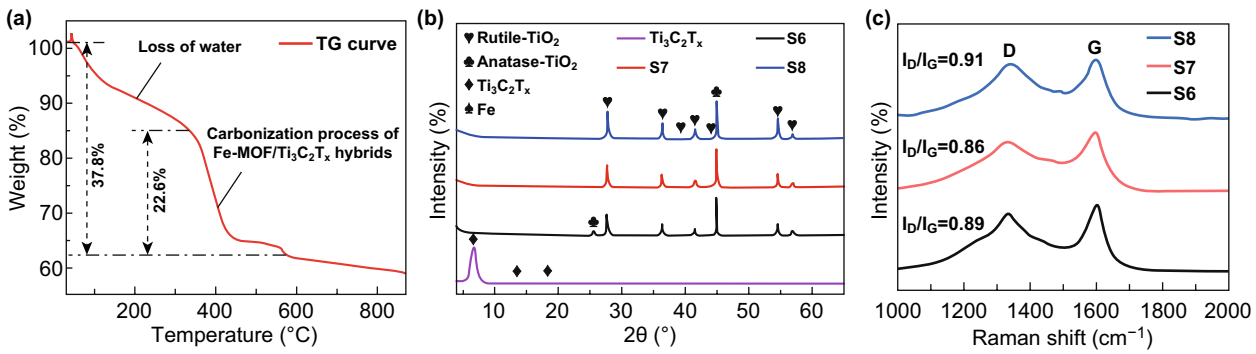

Fig. 2 **a** TG curve of as-prepared $Ti_3C_2T_x$–Fe-MOF hybrids. **b** XRD patterns of as-prepared $Ti_3C_2T_x$, S6, S7, and S8. **c** Raman spectra results of S6, S7, and S8

https://doi.org/10.1007/s40820-020-0398-2

demonstrated in Fig. 2b. The typical peaks corresponding to the (002), (004), and (006) planes of $Ti_3C_2T_x$ could be seen at 6.7°, 13.7°, and 18.7°, respectively, suggesting the successful synthesis of $Ti_3C_2T_x$ MXene [19, 50, 51]. It was seen that a small peak at 25.74° appeared after carbonizing at 600 °C, which was corresponding to the (101) plane of anatase-TiO_2 (JCPDS No. 75-1537). The other peaks at 27.7°, 36.3°, 41.5°, 54.5°, and 56.84° in the XRD pattern of S6 were assigned to the (110), (101), (111), (211), and (220) planes of the rutile-TiO_2 (JCPDS No. 78-1510). Moreover, the peak at 44.9° was indexed to the (110) plane of Fe (JCPDS No. 87-0722). As shown in Fig. 2b, the anatase phase disappeared when the temperature increased over 700 °C, which agreed with the results reported in other works [31, 52, 53]. With the temperature increasing to 800 °C, there were only rutile-TiO_2 and Fe phase remained in the sample. The phase fraction and averaged grain size of all the three samples (S6, S7, and S8) were calculated based on the XRD data by using Jade software with the WPF refinement, and the results are summarized in Table 1. The fractions of iron phase kept around 23% when the carbonization temperature increased from 600 to 800 °C, indicating the Fe element in Fe-MOFs was completely reduced and transformed into zerovalent metallic state by hydrogen. On the other hand, the sum of phase fractions of TiO_2 in all the three samples was close to 75%, suggesting the Ti element in $Ti_3C_2T_x$ sheets was in the form of TiO_2. The averaged grain size of rutile-TiO_2 increased from 40.1 to 57.6 nm with the increasing carbonizing temperature. The formation of rutile-TiO_2 and the disappearance of anatase-TiO_2 could be beneficial to the dielectric loss since the electromagnetic response of latter phase is worse than that of the former [53]. In addition, the XRD pattern of Ti_3AlC_2 is provided in Fig. S2. The Raman spectra of the three samples (S6, S7, and S8) are shown in Fig. 2c. The peaks, which corresponded to the characteristic D and G bands of carbon, appeared at 1343 and 1597 cm^{-1} in the Raman spectra of S6, S7, and S8. The intensities ratio between D and G (I_D/I_G) of S6, S7, and S8 was 0.89, 0.86, and 0.91, respectively. Generally, the descending value of I_D/I_G indicates that the amorphous carbon transforms into the ordered graphite carbon [28]. On the one hand, the decreasing I_D/I_G values for S6 to S7 samples could imply the improved carbon ordering with the increasing temperature. Normally, the amount of defects would be reduced with the increasing temperature, which led to the decreasing I_D/I_G value and the transformation from amorphous carbon to ordered carbon [54]. On the other hand, the I_D/I_G values showed an increasing tendency from S7 to S8. This result could be interpreted as being caused by an increase in the number, or in the size, of the graphitic domains [55–57]. It was worth mentioning that the increasing order of carbon is beneficial to increase the conductivity of carbon sheets, which could contribute to the conductive loss in EMW absorption process [35].

Table 1 Phase fraction and averaged grain size of S6, S7, and S8

Samples	Phase fraction (%)			Averaged grain size (nm)	
	Anatase	Rutile	Fe	Anatase	Rutile
S6	6.8 (0.8)	71.8 (4.8)	21.4 (1.4)	17.3	40.1 (9.6)
S7	–	75.2 (5.2)	24.8 (1.7)	–	52.4 (12.6)
S8	–	76.6 (5.3)	23.4 (1.6)	–	57.6 (11.5)

The typical layered structure of $Ti_3C_2T_x$ is clearly exhibited in Fig. 3a [51]. Additionally, the morphologies of S6, S7, and S8 observed by SEM are shown in Fig. 3b–d. The similar 2D laminated structure and small particles inserted between the layers were found in both S6 (Fig. 3b) and S7 (Fig. 3c). As for S8, it could be seen that the particles between layers grew significant and showed a high degree of aggregation in Fig. 3d. The EDS result for as-prepared $Ti_3C_2T_x$ presented that the residual Al element was only 2.8 wt%, which confirmed the successful etching of Ti_3AlC_2, as shown in Fig. S4. The element mapping analysis for S7 further illustrated the uniform distribution of the Fe, Ti, C, and O elements in the sandwich-like 2D Fe&TiO_2@C composites, as shown in Fig. S5. The TEM images of the $Ti_3C_2T_x$, as-synthesized S6, S7, and S8 are presented in Fig. 3e–h. Before the carbonization process, it was seen that the shuttle-like Fe-MOFs, whose size was about 200–300 nm in length and 100–150 nm in width, were distributed homogenously in the laminated thin $Ti_3C_2T_X$ sheets as shown in Fig. S3. After carbonating at 600 °C, the smooth $Ti_3C_2T_X$ sheets were transformed into coarse disordered carbon sheets while rectangle TiO_2 nanoparticles were precipitated. In addition, in our previous work, the microstructure evaluation of the Fe-MOFs during carbonization was studied [58]. Firstly, the Fe-MOFs transformed into Fe_3O_4 nanoparticles and porous carbon. Then, it began to collapse and transform into Fe nanoparticles with increasing the temperature. Due to the reduction atmosphere and relative longer carbonization time applied in this work, the

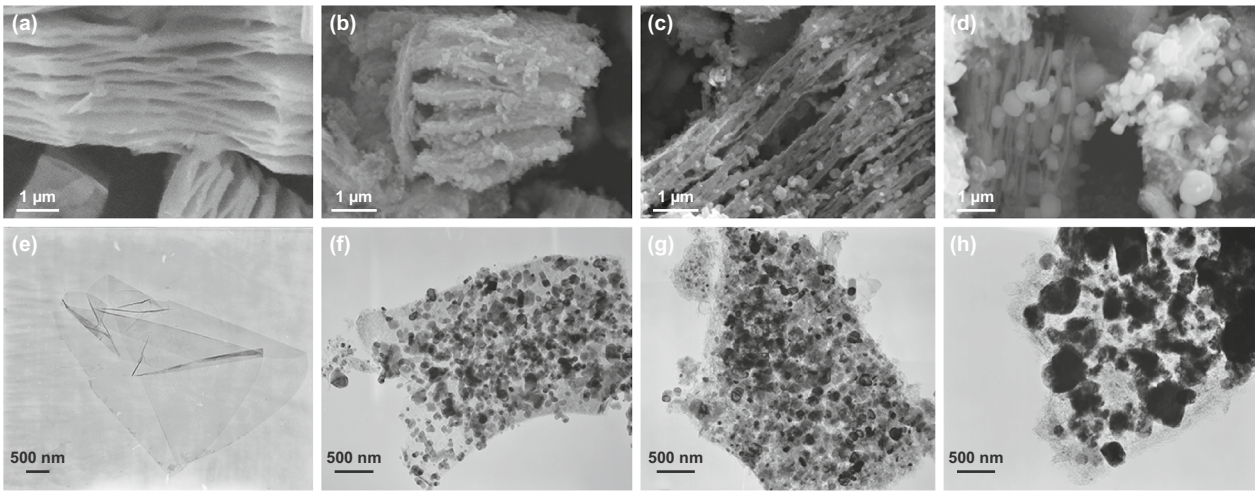

Fig. 3 SEM and TEM images of $Ti_3C_2T_x$ (**a**, **e**), S6 (**b**, **f**), S7 (**c**, **g**), and S8 (**e**, **h**)

Fe-MOFs decomposed into Fe nanoparticles wrapped by carbon, as shown in Fig. 3f. The Fe@C played an important role in improving impendence matching and providing interfacial polarization and magnetic loss. When the temperature increased to 700 °C, the size of the derived TiO_2 and Fe nanoparticles slightly increased, and the aggregation of nanoparticles also became more intense (Fig. 3g). Furthermore, the TiO_2 and Fe nanoparticles grew up excessively at 800 °C, which was consistent with the XRD results shown in Table 1, and ended up in oversized particles, as exhibited in Fig. 3h. This sandwich-like 2D laminated structure of Fe&TiO_2@C composites was beneficial to the absorption of EM energy [37, 53].

3.3 Electromagnetic Parameters and Microwave Absorption Performance

The electromagnetic absorption of Fe&TiO_2@C composites was determined by the relative complex permittivity (ε_r) and permeability (μ_r). Normally, the real parts of permittivity and permeability (ε' and μ') represent for the storage ability of electromagnetic energy, while the imaginary parts of those (ε'' and μ'') stand for the energy dissipation. Figure 4a, b shows the complex permittivity of Fe&TiO_2@C composites derived at different temperatures at the frequency ranging from 2 to 18 GHz. Both the real and imaginary parts of permittivity of Fe&TiO_2@C composites were enhanced with the increasing carbonizing temperatures. In detail, the ε' value of S6 maintained constant at around 6.0 within the whole frequency range, indicating the poor energy storage ability. However, S7 and S8 exhibited much higher value of ε' than S6 (~ 12 for S7 and ~ 13 for S8), which probably were resulted from the disappearance of the anatase-TiO_2 and the formation of more rutile-TiO_2 when the carbonating temperature reached over 600 °C according to the XRD results. Besides, the mildly enlarged ε' value of S7 and S8 within the frequency was also helpful for achieving excellent EMW absorption. Similarly, the ε'' value of S6 stayed around 0.5 while that of S7 declined from 4.7 to 3.5 and S8 slowly decreased from 7.2 and then mildly fluctuated at around 4.6. Compared with S6, the S7 and S8 with higher ε'' values exhibited stronger EMW attenuation ability. In addition, the ε' and ε'' plots of S7 exhibited an obvious fluctuation with the frequency ranging from 12 to 16 GHz, revealing the existence of polarization behavior. As for S6, the low graphitization degree, which was identified by the Raman spectra results, caused the low values of permittivity leading to the flat ε' and ε'' curves [59]. The ε' and ε'' curves for S8 at the frequency range of 12–16 GHz were mildly fluctuated, which could be attributed to the aggregation of nanoparticles hindering the polarization process. It was reasonable to assume that these dielectric properties mainly come from the polarization process, which were induced by the defects, the heterointerfaces, and the conductive carbon sheets existed in the Fe&TiO_2@C nanocomposites.

The magnetic hysteresis loops of all the three samples showed typical ferromagnetic features, as shown in Fig. S6a,

 https://doi.org/10.1007/s40820-020-0398-2

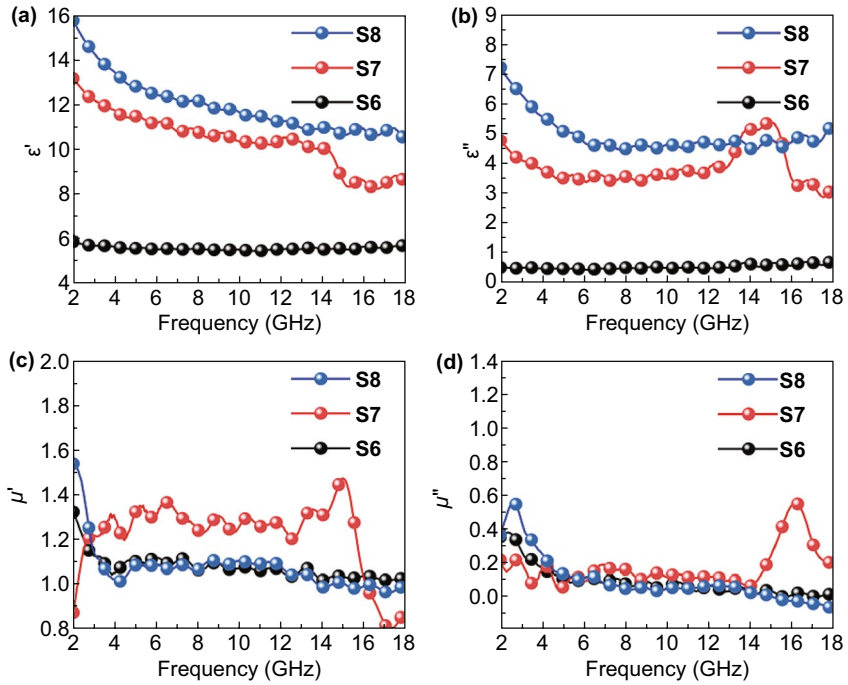

Fig. 4 Frequency dependences of **a** real and **b** imaginary parts of complex permittivity, **c** real and **d** imaginary parts of complex permeability for the S6, S7, and S8 at the frequency range of 2–18 GHz

b. The saturation magnetization (M_s) of 19.7, 29.3, and 28.7 emu g^{-1} and coercivity (H_c) of 72.7, 84.7, and 37.8 Oe were corresponded to the S6, S7, and S8, respectively. The μ' and μ'' of the samples in the frequency range of 2–18 GHz are shown in Fig. 4c, d. The μ' of S6 and S8 stayed at a value of 1.1 while S7 showed a relative higher value of 1.3 within the most of the measuring frequency range. In the frequency range of 2–6 GHz, some peaks for μ'' of S6 and S8 illustrated the existent of magnetic resonance behavior [60, 61]. Furthermore, the μ'' of S6 and S8 both decreased to nearly 0 when the frequency increased over 6 GHz, indicating the nature characteristic of the magnetic loss of S6 and S8 in the high frequency resulting from the Snoek's limitation of Fe [62]. In addition, the S8 exhibited negative values of μ'' in the frequency range of 15–18 GHz, which was normally attributed to the radiation of magnetic energy [63–65]. According to Maxwell equations, this phenomenon could be caused by the magnetic energy released from internal magnetic field, which was induced by the motion of charges in carbon frameworks under the alternating EM field. Unlike the former ones, the μ'' plot of S7 changed barely in the frequency range of 2–14 GHz, and a peak appeared at 16 GHz which was also attributed to magnetic resonance in high frequency range [61]. According to the above analyses, the S7 sample might perform better impendence matching and electromagnetic energy dissipation ability than both S6 and S8.

The dielectric loss tangent ($\tan\delta_\varepsilon = \varepsilon''/\varepsilon'$) of samples was calculated and is shown in Fig. 5a. Overall, the value of $\tan\delta_\varepsilon$ showed an increasing trend with the increasing carbonization temperatures from 600 to 800 °C. This could also be attributed to the formation of rutile-TiO_2 and defects when the treatment temperature increased over 600 °C. Generally, in the frequency range of 2–18 GHz, electronic polarization, Debye dipolar, and interfacial polarization and its related relaxation processes are the main sources of dielectric loss [9]. Firstly, the introduction of Fe nanoparticles, TiO_2 nanoparticles, and carbon nanosheets could form multiple interfaces, such as Fe–C, TiO_2–C and Fe–TiO_2, to generate interfacial polarization and related relaxation process. The interfacial polarization process as mentioned could cause the Maxwell–Wagner effect [42, 66], which contributed to the enhanced dielectric loss of Fe&TiO_2@C composites. The dipolar polarization was also one of the main factors to dissipate the EMW energy, since the Fe&TiO_2 nanoparticles and defects distributed on the carbon sheets would form dipoles.

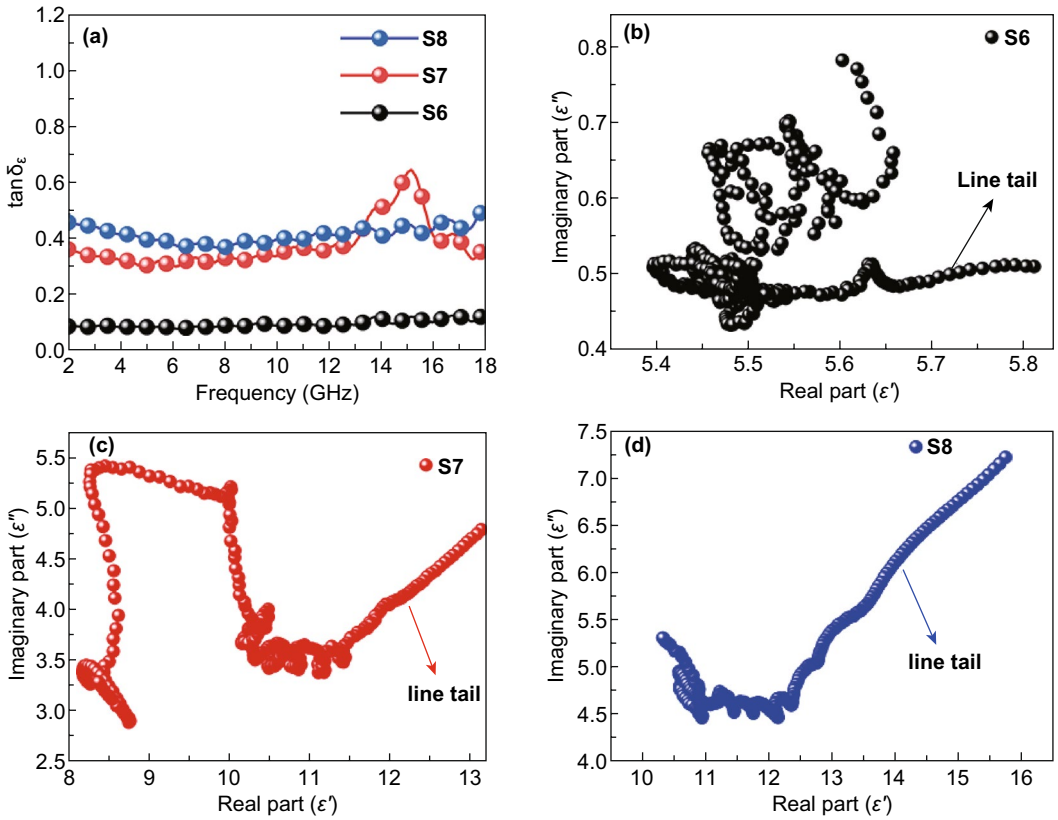

Fig. 5 **a** Dielectric loss tangent of S6, S7, and S8 from 2 to 18 GHz. Plots of ε' versus ε'' for **b** S6, **c** S7, and **d** S8

In order to further understand the polarization behavior during the EM absorption process, the plots of ε' versus ε'' of all three samples are drawn in Fig. 5b–d. Based on the Debye relaxation, the relationship between ε' and ε'' could be described as Eq. (1):

$$\left(\varepsilon' - \frac{\varepsilon_s + \varepsilon_\infty}{2}\right)^2 + \left(\varepsilon''\right)^2 = \left(\frac{\varepsilon_s - \varepsilon_\infty}{2}\right)^2 \quad (1)$$

where ε' and ε'' represent the real and imaginary part of permittivity, while ε_s and ε_∞ represent the static constant and the dielectric constant at infinite frequency, respectively. Hence, the semicircles in the plots of ε' versus ε'' could be signs for the presence of polarization process. As shown in Fig. 5b, there were several semicircles in the plot of S6, indicating the existence of polarization process. As for S7, it could be seen from Fig. 5c that multiple semicircles present in the frequency range of 6–18 GHz, which suggested the polarization processes happened among most of the tested frequency range [36, 67]. The plot of S8 also exhibited a lot of small semicircles in the frequency range of 8–18 GHz as shown in Fig. 5d. In addition, the observed semicircles for S6, S7, and S8 mostly appeared in frequency range of 10–18 GHz, suggesting that the polarization and related relaxation process occupied the dominate position in dielectric loss mechanism at high frequency range. These polarization processes may be caused by the diploes and interfaces existed in the Fe&TiO_2@C nanocomposites, which were beneficial to the EMW energy dissipation. Additionally, the conductive loss, which was mainly originated from the carbon nanosheets and Fe nanoparticles, could be confirmed by the presence of the line tails in the plots of ε' versus ε'' [39, 42]. Furthermore, the conduction loss also plays an important role in EMW attenuation. As shown in Fig. 5b, c, the length of line tail extended as the temperature increased, indicating that the conductive loss was gradually strengthened. Therefore, the above results revealed the existence of three main factors including dipole polarization relaxation, interfacial polarization relaxation, and conductive loss, which were in favor of the dielectric loss.

Besides the dielectric loss showing significant effects on EMW absorption, the magnetic loss also plays a key role in EMW absorption, which is theoretically originated from magnetic resonance, eddy current effect, and magnetic hysteresis [3, 9]. It is reasonable to exclude magnetic

 https://doi.org/10.1007/s40820-020-0398-2

hysteresis loss for the applied weak and relative high-frequency electromagnetic field [6]. Normally, the magnetic resonance can be divided into natural resonance and exchange resonance. The natural resonance often happens in the low frequency range (lower than 10 GHz), while the exchange resonance takes place at over 10 GHz range [3]. The calculated magnetic loss tangent ($\tan\delta_\mu = \mu''/\mu'$) of samples is shown in Fig. 6a. The $\tan\delta_\mu$ plots of S6 and S8 had a small peak at initial frequency range (2–4 GHz), which were assumed as a result of natural resonance, and they stayed around 0.05 in the frequency range of 5–18 GHz. As for the $\tan\delta_\mu$ plot of S7, it fluctuated mildly at low frequency range and kept around 0.05 in the range of 5–14 GHz. Then, the $\tan\delta_\mu$ plot of S7 exhibited a peak at high frequency range (14–18 GHz), whose apex exceeding 0.5 suggesting strong magnetic loss at related frequency range. Magnetic eddy current is another critical role for magnetic loss, which is inevitable in magnetic system. Such effect can be evaluated by $\mu''(\mu')^{-2}f^{-1}$, where μ' and μ'' represent the real and imaginary part of permittivity and f is the frequency of EM field, respectively. When there exists eddy current effect, the value of $\mu''(\mu')^{-2}f^{-1}$ will be a constant as the frequency is changing [6, 36, 68]. Otherwise, there exists other magnetic loss mechanism in the system. As shown in Fig. 6b, the $\mu''(\mu')^{-2}f^{-1}$ plots of S6 and S8 stayed as a constant from 8 to 18 GHz, and the $\mu''(\mu')^{-2}f^{-1}$ value of S7 was a constant at the range of 6–14 GHz. These results confirmed that the magnetic loss of Fe&TiO_2@C nanocomposites was mainly caused by eddy current effect within the tested frequency range. Additionally, the magnetic resonance, including natural and exchange resonance, also played an important role in magnetic loss based on the previous analysis of μ' and μ''.

The EM wave reflection loss (*RL*) values of the Fe&TiO_2@C nanocomposites were calculated based on the measured data of EM parameters as Eqs. (2) and (3) [69–71]:

$$RL\ (\mathrm{dB}) = 20\log\left|\frac{Z_{in} - Z_0}{Z_{in} + Z_0}\right| \quad (2)$$

where the input impedance Z_{in} of the absorber is given by the following equation:

$$Z_{in} = Z_0\sqrt{\mu_r/\varepsilon_r}\tanh\left|j\left(\frac{2\pi fd}{c}\right)\sqrt{\mu_r\varepsilon_r}\right| \quad (3)$$

where ε_r, μ_r, f, and d represent the complex permittivity and permeability of the EMW absorption materials, the related EM frequency, and the thickness of absorbers, respectively. Effective absorption bandwidth (*EAB*) is defined as the frequency range related to the *RL* value lower than − 10 dB, which indicates that more than 90% of the EM wave energy could be absorbed in this range. Figure 7a–c illustrates the 3D maps of *RL* data for S6, S7, and S8 at different thicknesses over 2–18 GHz. Besides, the ε' and ε'' (Fig. S7a, b), μ' and μ'' (Fig. S7c, d)), and *RL* results (Fig. S8) for Fe-MOFs and $Ti_3C_2T_x$ (MXene) after carbonized at 700 °C are shown in Supporting Information as comparison. S6 showed a weak EMW absorption performance, which could be related to its low dielectric and magnetic loss, while a maximum *EAB* of 6.5 GHz (from 11.5 to 18 GHz) with a matching thickness of only 1.6 mm was achieved for S7 sample. It can be further tuned to own a strong EMW absorption ability by changing its thickness. For example, its RL_{min} could reach − 41.5 dB at 10.1 GHz with an *EAB* of 3.2 GHz when thickness is

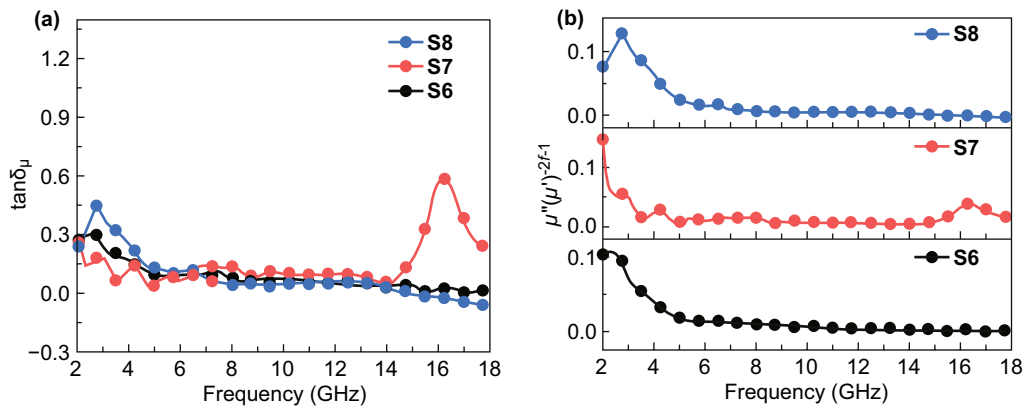

Fig. 6 **a** Magnetic loss tangent of S6, S7, and S8. **b** The calculated $\mu'(\mu'')^{-2}f^{-1}$ for S6, S7, and S8 at the frequency range of 2–18 GHz

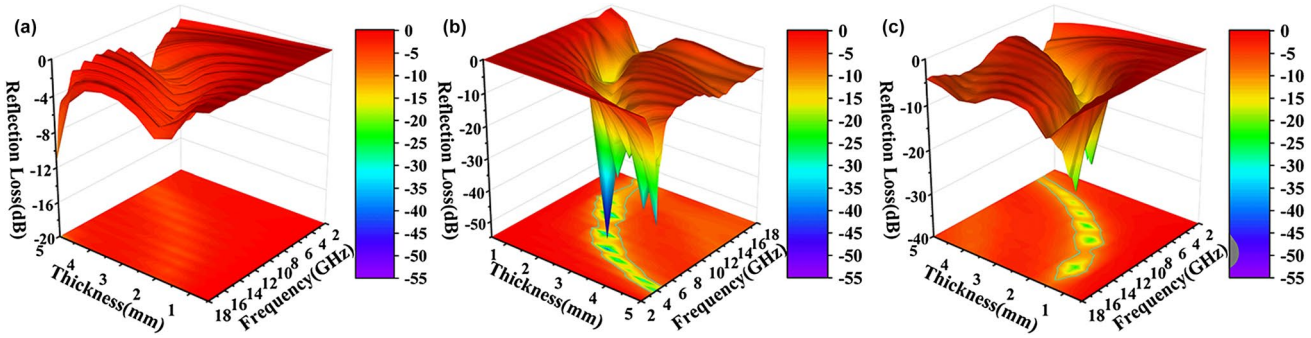

Fig. 7 3D maps of *RL* values for S6 (**a**), S7 (**b**), and S8 (**c**) at different thicknesses over 2–18 GHz

2.1 mm, and a −51.8 dB RL_{min} (at 6.6 GHz) could be obtained at thickness of 3.0 mm. Despite that the dielectric loss of S7 was not the biggest comparing with that of S6 and S8, it achieved a better EMW absorption performance than S8 sample, which was ascribed to the more uniform distribution of Fe and TiO_2 nanoparticles on the laminated carbon surfaces, leading to a better synergistic effect of dielectric and magnetic response [35–37]. In the case of S8, it also showed a relatively wide *EAB* of 5.0 GHz (from 12 to 17 GHz) with thickness of 1.6 mm, as shown in Fig. 7c. Though the S8 performed bigger dielectric loss and similar magnetic loss compared with S7, its EMW absorption performance was not ideal, since EMW absorption needs the synergy effort of impendence matching and attenuation ability for EM energy. In order to compare the EMW absorption performance obtained in current investigation and studies on MXene-based materials, the related results are summarized in Table 2. It is shown that the Fe&TiO_2@C composite derived at 700 °C owned tunable, lightweight, and broadband EM absorption performance compared with the other MXene and related materials reported in the studies.

Generally, two indispensable factors should be taken into consideration while aiming to achieve outstanding EMW absorption properties. The first is EMW attenuation capability of the absorption materials, and the second is the impedance matching. Normally, attenuation constant is used to qualify the EM energy attenuation ability of absorbers. Attenuation constants α of the samples, which are shown in Fig. 8a, can be calculated by Eq. (4) [67]:

$$\alpha = \frac{\sqrt{2}\pi f}{c}\sqrt{(\mu''\varepsilon'' - \mu'\varepsilon') + \sqrt{(\mu''\varepsilon'' - \mu'\varepsilon')^2 + (\mu''\varepsilon' + \mu'\varepsilon'')^2}} \quad (4)$$

Both S7 and S8 showed strong EMW attenuation capability in the high frequency range (12–18 GHz), while S6 exhibited a weak performance in the whole tested range (2–18 GHz). It is obviously that S7 possessed the best attenuation capability compared to the other samples, which was beneficial to enhance EM wave energy attenuation. The

Table 2 EMW absorption performance of MXene-based materials

Material	Loading ratio (wt%)	$RL < -10$ dB		RL_{min}		References
		Bandwidth (GHz)	d (mm)	Value (dB)	d (mm)	
$Ti_3C_2T_x$	50	6.8	2	−40	3	[8]
$Ti_3C_2T_x$-24	55	5	1.7	−42.5	1.7	[72]
$Ti_3C_2T_x$	55	2.8	1.8	−30	1.8	[32]
Annealed $Ti_3C_2T_x$	50	2.8	1.85	−48.4	1.7	[32]
TiO_2/C	45	5.6	1.7	−36	1.7	[53]
$TiO_2/Ti_3C_2T_x/Fe_3O_4$	–	2	1.9	−57.3	1.9	[6]
C/TiO_2/α–Fe	70	3.5	1.5	−45.1	3.5	[36]
Co/TiO_2–C	45	4.6	2	−41.1	3	[37]
Fe&TiO_2@C	40	6.5	1.6	−51.8	3	Our work

https://doi.org/10.1007/s40820-020-0398-2

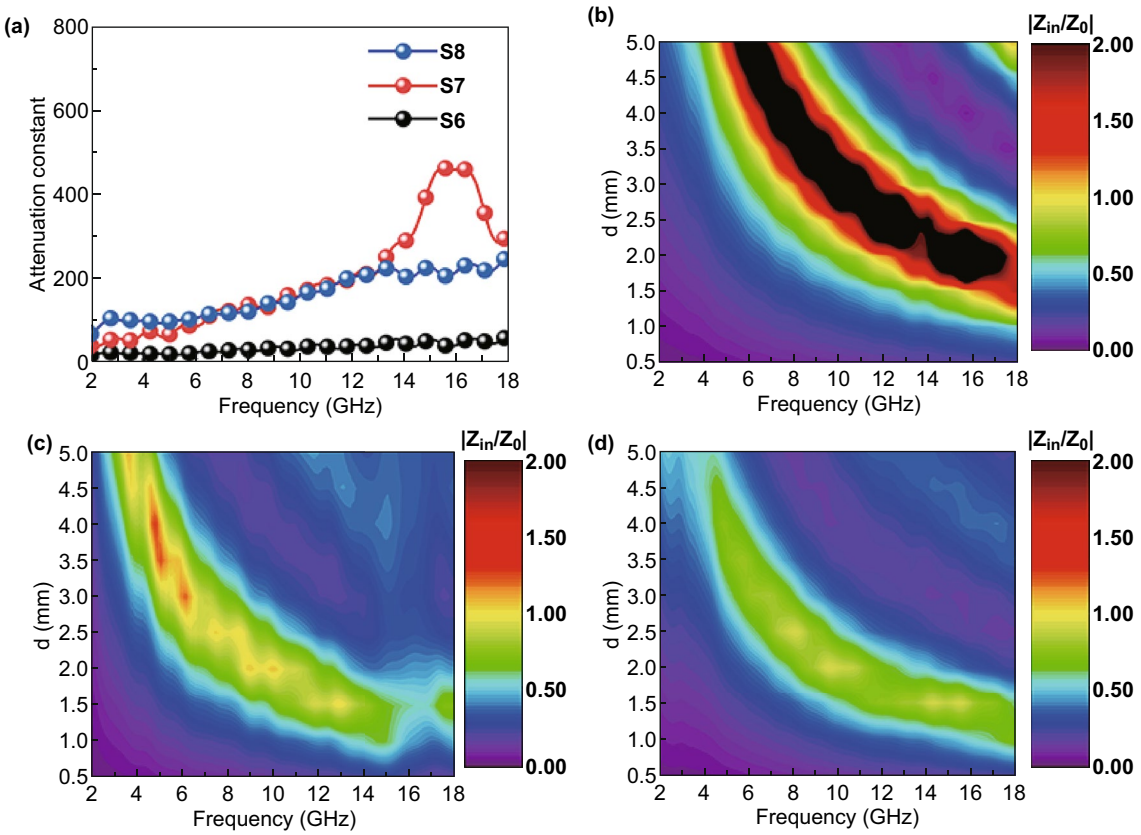

Fig. 8 **a** Attenuation constants results of S6, S7, and S8. 2D contour maps of $|Z_{in}/Z_0|$ at different thicknesses from 2 to 18 GHz for **b** S6, **c** S7, and **d** S8

uniform distribution of the Fe and TiO_2 nanoparticles and relative high graphitization degree of carbon sheets are the reasons for the high EM energy dissipation capability of S7. Conversely, the poor graphitization and formation of anatase-TiO_2 nanoparticles in S6 prevented it to achieve a high attenuation constant. The normalized characteristic impedance ($Z = |Z_{in}/Z_0|$) is used to evaluate the impedance matching of the samples, which is calculated based on Eq. (3). Normally, a good impedance matching means that the EMW could successfully enter the absorbers. To take sample thickness and measuring frequency into consideration, the 2D contour maps of Z for S6, S7, and S8 are exhibited in Fig. 8b–d. As is well known, achieving good impedance matching requires that the value of Z is equal or close to 1 [73, 74]. In Fig. 8b–d, the color of yellow represents the area in which Z equals 1, which representing the excellent impedance matching. The mismatch of impedance in S6 was apparent since the appearance of large black area, as shown in Fig. 8b. Compared with S6, the impedance matching for S7 and S8 showed a greatly improvement. Additionally, the yellow area of S7 was larger than that of S8, implying that S7 possessed a better impedance matching than S8. Overall, the S7 owned stronger EM energy attenuation ability and better impedance matching than the other two samples, leading to lightweight and broadband EM absorption performance of S7.

A possible EMW absorption mechanism for the sandwich-like laminated Fe&TiO_2@C nanocomposites is illustrated in Fig. 9. Firstly, the multiple reflections between the conductive carbon layers and scattering among the Fe and TiO_2 nanoparticles had taken place as soon as the EMW penetrated in the absorbers. These phenomena would be helpful in enhancing the EMW absorption efficiency. Additionally, the electron migration process including crossing and hoping over the conductive carbon sheets also played an important role in the EM energy attenuation. Secondly, dielectric loss produced by the polarization of dipoles and interfaces among the Fe, TiO_2, and carbon would give a great contribution to transform the EM

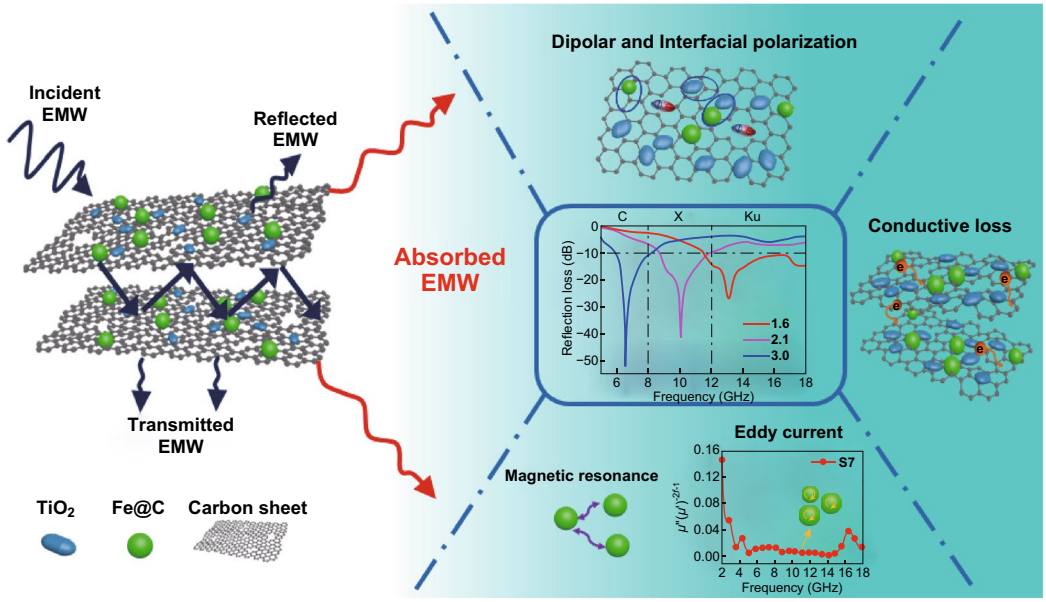

Fig. 9 Illustration of EMW absorption mechanisms for Fe&TiO_2@C nanocomposites

energy into thermal energy. In detail, the Fe, TiO_2 nanoparticles, and carbon sheets with different conductivity could form capacitor-like structure, such as the contact positions of carbon sheets, the interfaces of Fe–TiO_2, Fe–C, and TiO_2–C. These capacitor-like structures could give rise to the accumulation and rearrangement of space charge, resulting in generating vast interface polarization processes in alternating EM field [3, 75, 76]. Thus, the interfacial polarization played a main role in the EM attenuation process for this sandwich-like Fe&TiO_2@C ternary nanocomposite. Moreover, the magnetic loss caused by natural resonance, exchange resonance, and eddy current were inclined to enhance the EM energy dissipation ability of the laminated Fe&TiO_2@C nanocomposites. In addition, the improved impedance matching was achieved by introducing the rutile-TiO_2 and magnetic Fe nanoparticles through the in situ formation of Fe-MOFs followed by a suitable heat treatment. Based on the above discussion, it is highly expected that the laminated Fe&TiO_2@C nanocomposites could be a good candidate for high-performance EMW absorbing materials.

4 Conclusion

In summary, sandwich-like 2D laminated Fe&TiO_2@C nanocomposites with tunable EMW absorption performance have been synthesized from the MXene/MOFs precursors by the rapid microwave heating process followed by the carbonization process. The formation of Fe and rutile-TiO_2 nanoparticles sandwiched by the two-dimensional carbon nanosheets provided strong electromagnetic energy attenuation and good impedance matching for EMW absorption. The Fe&TiO_2@C nanocomposites exhibited a broad effective absorption bandwidth of 6.5 GHz (from 11.5 to 18 GHz) at a thickness of only 1.6 mm and the minimum *RL* value of − 51.8 dB at 6.6 GHz at a thickness of 3 mm, respectively. This work not only provides a good design and fabricating concept for the laminated metal and functional nanoparticles@C nanocomposites with good EMW absorption, but also offers an important guideline to fabricate various two-dimensional nanocomposites derived from the MXene precursors.

Acknowledgements This project was supported by the National Natural Science Foundation of China (Nos. 51971162, U1933112, 51671146), the Program of Shanghai Technology Research Leader (18XD1423800), and the Fundamental Research Funds for the Central Universities (22120180096).

Electronic supplementary material The online version of this article (https://doi.org/10.1007/s40820-020-0398-2) contains supplementary material, which is available to authorized users.

References

1. X. Sun, J. He, G. Li, J. Tang, T. Wang, Y. Guo, H. Xue, Laminated magnetic graphene with enhanced electromagnetic wave absorption properties. J. Mater. Chem. C **1**, 765–777 (2013). https://doi.org/10.1039/c2tc00159d
2. Y. Zhang, Y. Huang, T. Zhang, H. Chang, P. Xiao, H. Chen, Z. Huang, Y. Chen, Broadband and tunable high-performance microwave absorption of an ultralight and highly compressible graphene foam. Adv. Mater. **27**, 2049–2053 (2015). https://doi.org/10.1002/adma.201405788
3. M.S. Cao, Y.Z. Cai, P. He, J.C. Shu, W.Q. Cao, J. Yuan, 2D MXenes: electromagnetic property for microwave absorption and electromagnetic interference shielding. Chem. Eng. J. **359**, 1265–1302 (2019). https://doi.org/10.1016/j.cej.2018.11.051
4. Q. Liu, Q. Cao, H. Bi, C. Liang, K. Yuan, W. She, Y. Yang, R. Che, CoNi@SiO_2@TiO_2 and CoNi@Air@TiO_2 microspheres with strong wideband microwave absorption. Adv. Mater. **28**, 486–490 (2016). https://doi.org/10.1002/adma.201503149
5. H. Luo, W. Feng, C. Liao, L. Deng, S. Liu, H. Zhang, P. Xiao, Peaked dielectric responses in Ti_3C_2 MXene nanosheets enabled composites with efficient microwave absorption. J. Appl. Phys. **123**, 104103 (2018). https://doi.org/10.1063/1.5008323
6. P. Liu, Z. Yao, V.M.H. Ng, J. Zhou, L.B. Kong, K. Yue, Facile synthesis of ultrasmall Fe_3O_4 nanoparticles on MXenes for high microwave absorption performance. Compos. Part A-Appl. Sci. **115**, 371–382 (2018). https://doi.org/10.1016/j.compositesa.2018.10.014
7. C. Wang, X. Han, P. Xu, X. Zhang, Y. Du, S. Hu, J. Wang, X. Wang, The electromagnetic property of chemically reduced graphene oxide and its application as microwave absorbing material. Appl. Phys. Lett. **98**, 072906 (2011). https://doi.org/10.1063/1.3555436
8. W. Feng, H. Luo, Y. Wang, S. Zeng, L. Deng, X. Zhou, H. Zhang, S. Peng, Ti_3C_2 MXene: a promising microwave absorbing material. RSC Adv. **8**, 2398–2403 (2018). https://doi.org/10.1039/c7ra12616f
9. M.S. Cao, J.C. Shu, X.X. Wang, X. Wang, M. Zhang, H.J. Yang, X.Y. Fang, J. Yuan, Electronic structure and electromagnetic properties for 2D electromagnetic functional materials in gigahertz frequency. Ann. Phys. (2019). https://doi.org/10.1002/andp.201800390
10. Y. Zhang, Y. Huang, H. Chen, Z. Huang, Y. Yang, P. Xiao, Y. Zhou, Y. Chen, Composition and structure control of ultralight graphene foam for high-performance microwave absorption. Carbon **105**, 438–447 (2016). https://doi.org/10.1016/j.carbon.2016.04.070
11. M. Cao, C. Han, X. Wang, M. Zhang, Y. Zhang et al., Graphene nanohybrids: excellent electromagnetic properties for the absorbing and shielding of electromagnetic waves. J. Mater. Chem. C **6**, 4586–4602 (2018). https://doi.org/10.1039/c7tc05869a
12. T. Chen, F. Deng, J. Zhu, C. Chen, G. Sun, S. Ma, X. Yang, Hexagonal and cubic Ni nanocrystals grown on graphene: phase-controlled synthesis, characterization and their enhanced microwave absorption properties. J. Mater. Chem. **22**, 15190–15197 (2012). https://doi.org/10.1039/c2jm31171b
13. J. Ma, X. Wang, W. Cao, C. Han, H. Yang, J. Yuan, M. Cao, A facile fabrication and highly tunable microwave absorption of 3D flower-like Co_3O_4–rGO hybrid-architectures. Chem. Eng. J. **339**, 487–498 (2018). https://doi.org/10.1016/j.cej.2018.01.152
14. W. Feng, Y. Wang, J. Chen, L. Wang, L. Guo, J. Ouyang, D. Jia, Y. Zhou, Reduced graphene oxide decorated with in situ growing ZnO nanocrystals: facile synthesis and enhanced microwave absorption properties. Carbon **108**, 52–60 (2016). https://doi.org/10.1016/j.carbon.2016.06.084
15. O. Mashtalir, M. Naguib, V.N. Mochalin, Y. Dall'Agnese, M. Heon, M.W. Barsoum, Y. Gogotsi, Intercalation and delamination of layered carbides and carbonitrides. Nat. Commun. **4**, 1–7 (2013). https://doi.org/10.1038/ncomms2664
16. B. Anasori, M.R. Lukatskaya, Y. Gogotsi, 2D metal carbides and nitrides (MXenes) for energy storage. Nat. Rev. Mater. **2**, 16098 (2017). https://doi.org/10.1038/natrevmats.2016.98
17. M. Naguib, M. Kurtoglu, V. Presser, J. Lu, J. Niu et al., Two-dimensional nanocrystals produced by exfoliation of Ti_3AlC_2. Adv. Mater. **23**, 4248–4253 (2011). https://doi.org/10.1002/adma.201102306
18. M. Naguib, O. Mashtalir, J. Carle, V. Presser, J. Lu, L. Hultman, Y. Gogotsi, M.W. Barsoum, Two-dimensional transition metal carbides. ACS Nano **6**, 1322–1331 (2012). https://doi.org/10.1021/nn204153h
19. M. Ghidiu, M.R. Lukatskaya, M.-Q. Zhao, Y. Gogotsi, M.W. Barsoum, Conductive two-dimensional titanium carbide 'clay' with high volumetric capacitance. Nature **516**, 78–81 (2014). https://doi.org/10.1038/nature13970
20. S. Xu, G. Wei, J. Li, Y. Ji, N. Klyui, V. Izotov, W. Han, Binder-free $Ti_3C_2T_x$ MXene electrode film for supercapacitor produced by electrophoretic deposition method. Chem. Eng. J. **317**, 1026–1036 (2017). https://doi.org/10.1016/j.cej.2017.02.144
21. Y. Xia, T.S. Mathis, M.Q. Zhao, B. Anasori, A. Dang et al., Thickness-independent capacitance of vertically aligned liquid-crystalline MXenes. Nature **557**, 409–412 (2018). https://doi.org/10.1038/s41586-018-0109-z

22. L. Zhou, X. Zhang, L. Ma, J. Gao, Y. Jiang, Acetylcholinesterase/chitosan-transition metal carbides nanocomposites-based biosensor for the organophosphate pesticides detection. Biochem. Eng. J. **128**, 243–249 (2017). https://doi.org/10.1016/j.bej.2017.10.008
23. X. Zhu, B. Liu, H. Hou, Z. Huang, K.M. Zeinu et al., Alkaline intercalation of Ti_3C_2 MXene for simultaneous electrochemical detection of Cd(II), Pb(II), Cu(II) and Hg(II). Electrochim. Acta **248**, 46–57 (2017). https://doi.org/10.1016/j.electacta.2017.07.084
24. M.A. Faisal Shahzad, C.B. Hatter, B. Anasori, S.M. Hong, C.M. Koo, Y. Gogotsi, Electromagnetic interference shielding with 2D transition metal carbides (MXenes). Science **353**, 1137–1140 (2016). https://doi.org/10.1126/science.aag2421
25. W. Cao, C. Ma, S. Tan, M. Ma, P. Wan, F. Chen, Ultrathin and flexible CNTs/MXene/cellulose nanofibrils composite paper for electromagnetic interference shielding. Nano-Micro Lett. **11**, 72 (2019). https://doi.org/10.1007/s40820-019-0304-y
26. G. Xu, X. Wang, S. Gong, S. Wei, J. Liu, Y. Xu, Solvent-regulated preparation of well-intercalated $Ti_3C_2T_x$ MXene nanosheets and application for highly effective electromagnetic wave absorption. Nanotechnology **29**, 355201 (2018). https://doi.org/10.1088/1361-6528/aac8f6
27. M.A. Hope, A.C. Forse, K.J. Griffith, M.R. Lukatskaya, M. Ghidiu, Y. Gogotsi, C.P. Grey, NMR reveals the surface functionalisation of Ti_3C_2 MXene. Phys. Chem. Chem. Phys. **18**, 5099–5102 (2016). https://doi.org/10.1039/c6cp00330c
28. X. Sang, Y. Xie, M.W. Lin, M. Alhabeb, K.L. Van Aken et al., Atomic defects in monolayer titanium carbide ($Ti_3C_2T_x$) MXene. ACS Nano **10**, 9193–9200 (2016). https://doi.org/10.1021/acsnano.6b05240
29. P. He, M.S. Cao, J.C. Shu, Y.Z. Cai, X.X. Wang, Q.L. Zhao, J. Yuan, Atomic layer tailoring titanium carbide MXene to tune transport and polarization for utilization of electromagnetic energy beyond solar and chemical energy. ACS Appl. Mater. Interfaces **11**, 12535–12543 (2019). https://doi.org/10.1021/acsami.9b00593
30. W. Feng, H. Luo, S. Zeng, C. Chen, L. Deng et al., Ni-modified Ti_3C_2 MXene with enhanced microwave absorbing ability. Mater. Chem. Front. **2**, 2320–2326 (2018). https://doi.org/10.1039/c8qm00436f
31. X. Li, X. Yin, M. Han, C. Song, X. Sun, H. Xu, L. Cheng, L. Zhang, A controllable heterogeneous structure and electromagnetic wave absorption properties of Ti_2CT_x MXene. J. Mater. Chem. C **5**, 7621–7628 (2017). https://doi.org/10.1039/c7tc01991b
32. M. Han, X. Yin, H. Wu, Z. Hou, C. Song, X. Li, L. Zhang, L. Cheng, Ti_3C_2 MXenes with modified surface for high-performance electromagnetic absorption and shielding in the X-band. ACS Appl. Mater. Interfaces **8**, 21011–21019 (2016). https://doi.org/10.1021/acsami.6b06455
33. J. Qiao, X. Zhang, D. Xu, L. Kong, L. Lv, F. Yang, F. Wang, W. Liu, J. Liu, Design and synthesis of TiO_2/Co/carbon nanofibers with tunable and efficient electromagnetic absorption. Chem. Eng. J. **380**, 122591 (2020). https://doi.org/10.1016/j.cej.2019.122591
34. N. Wu, C. Liu, D. Xu, J. Liu, W. Liu et al., Ultrathin high-performance electromagnetic wave absorbers with facilely fabricated hierarchical porous Co/C crabapples. J. Mater. Chem. C **7**, 1659–1669 (2019). https://doi.org/10.1039/c8tc04984j
35. W. Feng, H. Luo, Y. Wang, S. Zeng, Y. Tan et al., Mxenes derived laminated and magnetic composites with excellent microwave absorbing performance. Sci. Rep. **9**, 3957 (2019). https://doi.org/10.1038/s41598-019-40336-9
36. G. Zhao, H. Lv, Y. Zhou, X. Zheng, C. Wu, C. Xu, Self-assembled sandwich-like MXene-derived nanocomposites for enhanced electromagnetic wave absorption. ACS Appl. Mater. Interfaces **10**, 42925–42932 (2018). https://doi.org/10.1021/acsami.8b16727
37. Q. Liao, M. He, Y. Zhou, S. Nie, Y. Wang et al., Rational construction of $Ti_3C_2T_x$/Co–MOF-derived laminated Co/TiO_2–C hybrids for enhanced electromagnetic wave absorption. Langmuir **34**, 15854–15863 (2018). https://doi.org/10.1021/acs.langmuir.8b03238
38. W. Xia, A. Mahmood, R. Zou, Q. Xu, Metal–organic frameworks and their derived nanostructures for electrochemical energy storage and conversion. Energy Environ. Sci. **8**, 1837–1866 (2015). https://doi.org/10.1039/c5ee00762c
39. W. Liu, L. Liu, G. Ji, D. Li, Y. Zhang, J. Ma, Y. Du, Composition design and structural characterization of MOF-derived composites with controllable electromagnetic properties. ACS Sustain. Chem. Eng. **5**, 7961–7971 (2017). https://doi.org/10.1021/acssuschemeng.7b01514
40. K. Wang, Y. Chen, R. Tian, H. Li, Y. Zhou, H. Duan, H. Liu, Porous Co–C core-shell nanocomposites derived from Co–MOF-74 with enhanced electromagnetic wave absorption performance. ACS Appl. Mater. Interfaces **10**, 11333–11342 (2018). https://doi.org/10.1021/acsami.8b00965
41. J. Xiong, Z. Xiang, J. Zhao, L. Yu, E. Cui et al., Layered NiCo alloy nanoparticles/nanoporous carbon composites derived from bimetallic MOFs with enhanced electromagnetic wave absorption performance. Carbon **154**, 391–401 (2019). https://doi.org/10.1016/j.carbon.2019.07.096
42. Z. Xiang, Y. Song, J. Xiong, Z. Pan, X. Wang et al., Enhanced electromagnetic wave absorption of nanoporous Fe_3O_4@carbon composites derived from metal–organic frameworks. Carbon **142**, 20–31 (2019). https://doi.org/10.1016/j.carbon.2018.10.014
43. X. Zhang, J. Qiao, J. Zhao, D. Xu, F. Wang et al., High-efficiency electromagnetic wave absorption of cobalt-decorated NH_2–UIO-66-derived porous ZrO_2/C. ACS Appl. Mater. Interfaces **11**, 35959–35968 (2019). https://doi.org/10.1021/acsami.9b10168
44. C. Zhou, C. Wu, D. Liu, M. Yan, Metal–organic framework derived hierarchical Co/C@V_2O_3 hollow spheres as a thin, lightweight, and high-efficiency electromagnetic wave absorber. Chem (Easton) **25**, 2234–2241 (2019). https://doi.org/10.1002/chem.201805565
45. S. Wang, Y. Xu, R. Fu, H. Zhu, Q. Jiao et al., Rational construction of hierarchically porous Fe–Co/N-doped carbon/rGO composites for broadband microwave absorption.

 https://doi.org/10.1007/s40820-020-0398-2

Nano-Micro Lett. **11**, 76 (2019). https://doi.org/10.1007/s40820-019-0307-8

46. W. Liu, Q. Shao, G. Ji, X. Liang, Y. Cheng, B. Quan, Y. Du, Metal–organic-frameworks derived porous carbon-wrapped Ni composites with optimized impedance matching as excellent lightweight electromagnetic wave absorber. Chem. Eng. J. **313**, 734–744 (2017). https://doi.org/10.1016/j.cej.2016.12.117
47. Y. Lu, Y. Wang, H. Li, Y. Lin, Z. Jiang, Z. Xie, Q. Kuang, L. Zheng, MOF-derived porous Co/C nanocomposites with excellent electromagnetic wave absorption properties. ACS Appl. Mater. Interfaces **7**, 13604–13611 (2015). https://doi.org/10.1021/acsami.5b03177
48. Z. Li, X. Han, Y. Ma, D. Liu, Y. Wang, P. Xu, C. Li, Y. Du, MOFs-derived hollow Co/C microspheres with enhanced microwave absorption performance. ACS Sustain. Chem. Eng. **6**, 8904–8913 (2018). https://doi.org/10.1021/acssuschemeng.8b01270
49. J. Wang, C. Xue, W. Yao, J. Liu, X. Gao et al., MOF-derived hollow TiO_2@C/$FeTiO_3$ nanoparticles as photoanodes with enhanced full spectrum light PEC activities. Appl. Catal. B-Environ. **250**, 369–381 (2019). https://doi.org/10.1016/j.apcatb.2019.03.002
50. F. Liu, A. Zhou, J. Chen, J. Jia, W. Zhou, L. Wang, Q. Hu, Preparation of Ti_3C_2 and Ti_2C MXenes by fluoride salts etching and methane adsorptive properties. Appl. Surface Sci. **416**, 781–789 (2017). https://doi.org/10.1016/j.apsusc.2017.04.239
51. M. Alhabeb, K. Maleski, B. Anasori, P. Lelyukh, L. Clark, S. Sin, Y. Gogotsi, Guidelines for synthesis and processing of two-dimensional titanium carbide ($Ti_3C_2T_x$ MXene). Chem. Mater. **29**, 7633–7644 (2017). https://doi.org/10.1021/acs.chemmater.7b02847
52. D.A.H. Hanaor, C.C. Sorrell, Review of the anatase to rutile phase transformation. J. Mater. Sci. **46**, 855–874 (2010). https://doi.org/10.1007/s10853-010-5113-0
53. M. Han, X. Yin, X. Li, B. Anasori, L. Zhang, L. Cheng, Y. Gogotsi, Laminated and two-dimensional carbon-supported microwave absorbers derived from MXenes. ACS Appl. Mater. Interfaces **9**, 20038–20045 (2017). https://doi.org/10.1021/acsami.7b04602
54. N. Wu, D. Xu, Z. Wang, F. Wang, J. Liu et al., Achieving superior electromagnetic wave absorbers through the novel metal–organic frameworks derived magnetic porous carbon nanorods. Carbon **145**, 433–444 (2019). https://doi.org/10.1016/j.carbon.2019.01.028
55. R.O. Dillon, J.A. Woollam, V. Katkanant, Use of Raman scattering to investigate disorder and crystallite formation in as-deposited and annealed carbon films. Phys. Rev. B **29**, 3482–3489 (1984). https://doi.org/10.1103/PhysRevB.29.3482
56. J. Jiu, H. Wang, C. Cao, H. Zhu, The effect of annealing temperature on the structure of diamond-like carbon films byelectrodeposition technique. J. Mater. Sci. **34**, 5205–5209 (1999). https://doi.org/10.1023/a:1004711913325
57. G.M.M.M. Lacerda, F.L. Freire Jr., Raman spectroscopy of annealed carbon nitride films deposited by RF-magnetron sputtering. Diam. Relat. Mater. **7**, 412–416 (1998). https://doi.org/10.1016/S0925-9635(97)00230-6
58. Z. Xiang, J. Xiong, B. Deng, E. Cui, L. Yu et al., Rational design of 2D hierarchically laminated Fe_3O_4@NPC@rGO nanocomposites with strong magnetic coupling for excellent electromagnetic absorption applications. J. Mater. Chem. C **8**, 2123–2134 (2020). https://doi.org/10.1039/c9tc06526a
59. X. Li, E. Cui, Z. Xiang, L. Yu, J. Xiong, F. Pan, W. Lu, Fe@NPC@CF nanocomposites derived from Fe–MOFs/biomass cotton for lightweight and high-performance electromagnetic wave absorption applications. J. Alloy. Compd. **819**, 152952 (2020). https://doi.org/10.1016/j.jallcom.2019.152952
60. L. Yan, J. Liu, S. Zhao, B. Zhang, Z. Gao et al., Coaxial multi-interface hollow Ni–Al_2O_3–ZnO nanowires tailored by atomic layer deposition for selective-frequency absorptions. Nano Res. **10**, 1595–1607 (2016). https://doi.org/10.1007/s12274-016-1302-8
61. Y. Zhang, X. Wang, M. Cao, Confinedly implanted $NiFe_2O_4$-rGO: cluster tailoring and highly tunable electromagnetic properties for selective-frequency microwave absorption. Nano Res. **11**, 1426–1436 (2018). https://doi.org/10.1007/s12274-017-1758-1
62. J. Shen, Y. Yao, Y. Liu, J. Leng, Tunable hierarchical Fe nanowires with a facile template-free approach for enhanced microwave absorption performance. J. Mater. Chem. C **4**, 7614–7621 (2016). https://doi.org/10.1039/c6tc01912a
63. J. Xiang, J. Li, X. Zhang, Q. Ye, J. Xu, X. Shen, Magnetic carbon nanofibers containing uniformly dispersed Fe/Co/Ni nanoparticles as stable and high-performance electromagnetic wave absorbers. J. Mater. Chem. A **2**, 16905–16914 (2014). https://doi.org/10.1039/c4ta03732d
64. D. Liu, Y. Du, Z. Li, Y. Wang, P. Xu et al., Facile synthesis of 3D flower-like Ni microspheres with enhanced microwave absorption properties. J. Mater. Chem. C **6**, 9615–9623 (2018). https://doi.org/10.1039/c8tc02931h
65. Z. Xu, Y. Du, D. Liu, Y. Wang, W. Ma, Y. Wang, P. Xu, X. Han, Pea-like Fe/Fe_3C nanoparticles embedded in nitrogen-doped carbon nanotubes with tunable dielectric/magnetic loss and efficient electromagnetic absorption. ACS Appl. Mater. Interfaces **11**, 4268–4277 (2019). https://doi.org/10.1021/acsami.8b19201
66. Y. Lin, J. Dai, H. Yang, L. Wang, F. Wang, Graphene multi-layered sheets assembled by porous $Bi_2Fe_4O_9$ microspheres and the excellent electromagnetic wave absorption properties. Chem. Eng. J. **334**, 1740–1748 (2018). https://doi.org/10.1016/j.cej.2017.11.150
67. D. Ding, Y. Wang, X. Li, R. Qiang, P. Xu, W. Chu, X. Han, Y. Du, Rational design of core-shell Co@C microspheres for high-performance microwave absorption. Carbon **111**, 722–732 (2017). https://doi.org/10.1016/j.carbon.2016.10.059
68. X. Wang, F. Pan, Z. Xiang, Q. Zeng, K. Pei, R. Che, W. Lu, Magnetic vortex core-shell Fe_3O_4@C nanorings with enhanced microwave absorption performance. Carbon **157**, 130–139 (2020). https://doi.org/10.1016/j.carbon.2019.10.030
69. T. Kim, J. Lee, K. Lee, B. Park, B.M. Jung, S.B. Lee, Magnetic and dispersible FeCoNi-graphene film produced without

heat treatment for electromagnetic wave absorption. Chem. Eng. J. **361**, 1182–1189 (2019). https://doi.org/10.1016/j.cej.2018.12.172

70. H.-B. Zhao, J.-B. Cheng, J.-Y. Zhu, Y.-Z. Wang, Ultralight CoNi/rGO aerogels toward excellent microwave absorption at ultrathin thickness. J. Mater. Chem. C **7**, 441–448 (2019). https://doi.org/10.1039/c8tc05239e
71. Y. Wang, X. Gao, C. Lin, L. Shi, X. Li, G. Wu, Metal organic frameworks-derived Fe-Co nanoporous carbon/graphene composite as a high-performance electromagnetic wave absorber. J. Alloys Compound. **785**, 765–773 (2019). https://doi.org/10.1016/j.jallcom.2019.01.271
72. Y. Tong, M. He, Y. Zhou, X. Zhong, L. Fan, T. Huang, Q. Liao, Y. Wang, Electromagnetic wave absorption properties in the centimetre-band of $Ti_3C_2T_x$ MXenes with diverse etching time. J. Mater. Sci.: Mater. Electron. **29**, 8078–8088 (2018). https://doi.org/10.1007/s10854-018-8814-9
73. X. Zhang, G. Ji, W. Liu, B. Quan, X. Liang, C. Shang, Y. Cheng, Y. Du, Thermal conversion of an Fe_3O_4@metal–organic framework: a new method for an efficient Fe–Co/nanoporous carbon microwave absorbing material. Nanoscale **7**, 12932–12942 (2015). https://doi.org/10.1039/c5nr03176a
74. Z. Xiang, B. Deng, C. Huang, Z. Liu, Y. Song, W. Lu, Rational design of hollow nanosphere γ-Fe_2O_3/MWCNTs composites with enhanced electromagnetic wave absorption. J. Alloys Compd. **822**, 153570 (2020). https://doi.org/10.1016/j.jallcom.2019.153570
75. M.M. Lu, W.Q. Cao, H.L. Shi, X.Y. Fang, J. Yang et al., Multi-wall carbon nanotubes decorated with ZnO nanocrystals: mild solution-process synthesis and highly efficient microwave absorption properties at elevated temperature. J. Mater. Chem. A **2**, 10540–10547 (2014). https://doi.org/10.1039/c4ta01715c
76. D. Zhang, T. Liu, J. Cheng, Q. Cao, G. Zheng, S. Liang, H. Wang, M.S. Cao, Lightweight and high-performance microwave absorber based on 2D WS_2–RGO Heterostructures. Nano-Micro Lett. **11**, 38 (2019). https://doi.org/10.1007/s40820-019-0270-4

 https://doi.org/10.1007/s40820-020-0398-2